Published in final edited form as:

Invest Radiol. 2021 April 01; 56(4): 197–206. doi:10.1097/RLI.0000000000000728.

A Targeted Molecular Localization Imaging Method Applied to Tumor Microvasculature

Feifei Zhao, Ph.D.,
Department of Biomedical Engineering, University of Virginia, Charlottesville, VA 22908, USA

Sunil Unnikrishnan, Ph.D.,
Department of Biomedical Engineering, University of Virginia, Charlottesville, VA 22908, USA

Elizabeth B. Herbst, B.Sc.,
Department of Biomedical Engineering, University of Virginia, Charlottesville, VA 22908, USA

Alexander L. Klibanov, Ph.D. [Associate Professor],
Division of Cardiovascular Medicine, Cardiovascular Research Center and Department of Biomedical Engineering, University of Virginia, Charlottesville, VA 22908, USA

F. William Mauldin Jr., Ph.D. [Assistant Research Professor],
Department of Biomedical Engineering, University of Virginia, Charlottesville, VA 22908, USA

John A. Hossack, Ph.D. [Professor]
Department of Biomedical Engineering, University of Virginia, Charlottesville, VA 22908, USA

Abstract

Objectives: Ultrasound contrast agents, consisting of gas filled microbubbles (MBs), have been imaged using several techniques that include ultrasound localization microscopy (ULM) and targeted molecular imaging (USMI). Each of these techniques aims to provide indicators of the disease state but has traditionally been performed independently without co-localization of molecular markers and super-resolved vessels. In this paper, we present a new imaging technology: a targeted molecular localization (TML) approach, which employs a single imaging sequence and reconstruction approach to co-localize super resolved vasculature with molecular imaging signature to provide simultaneous anatomic and biological information for potential multi-scale disease evaluation.

Materials and Methods: The feasibility of the proposed TML technique was validated in a murine hindlimb tumor model. TML imaging was performed on three groups that include: control tissue (leg), tumor tissue, and tumor tissue following sunitinib anti-vascular treatment. Quantitative measures for vessel index (VI) and molecular index (MI_{TML}) were calculated from the microvasculature and TML images, respectively. In addition to these conventional metrics, a new metric unique to the TML technique, reporting the ratio of targeted molecular index to vessel surface (MVR), was assessed.

Correspondence to: **John A. Hossack**, *PhD, Department of Biomedical Engineering, University of Virginia, Mail: 415 Lane Road, MR5 Building, Room 2121, Charlottesville, VA 22908, USA, Phone: (434) 243-5866; Fax: (434) 982-3870;* jh7fj@virginia.edu.

Results: The quantitative resolution results of the TML approach showed resolved resolution of the microvasculature down to 28.8 μm. VI increased in tumors with and without sunitinib compared to the control leg but the trend was not statistically significant. A decrease in MI_{TML} was observed for the tumor after treatment ($P < 0.0005$) and for the control leg ($P < 0.005$) compared with the tumor prior to treatment. Statistical differences in MVR were found between all groups: the control leg and tumor ($P < 0.05$), the control leg and tumor after sunitinib treatment ($P < 0.05$), and between tumors with and without sunitinib treatment ($P < 0.001$).

Conclusions: These findings validated the technical feasibility of the TML method and pre-clinical feasibility for differentiating between the normal and diseased tissue states.

Keywords

super resolution; molecular imaging; targeted microbubbles; co-localization; tumor

2. Introduction

Ultrasound contrast agents, composed of gas filled microbubbles (MBs), have been used in ultrasound contrast imaging over the past three decades to benefit many useful techniques. Ultrasound localization microscopy (ULM) is a rapidly growing field in recent years that enables super resolution ultrasound imaging [1–3]. ULM takes advantage of free-moving MBs as stochastic intravascular localized acoustic sources. By detecting and accumulating the positions of the individual MBs from different frames, it can resolve microvessels beyond the resolution limits of ultrasonic wave diffraction. Additionally, by tracking individual MBs, ULM can also be used to obtain microvascular flow velocity information [4–6]. Since the introduction of the ULM technique, it has found applications in microvascular imaging of several different organs including the kidney [4], thyroid [7], brain [2,8], prostate[9] and various tumor [10,11].

Ultrasound molecular imaging (USMI) uses molecularly targeted MBs to bind to specific disease markers that include inflammation, thrombosis, biofilm, and angiogenesis [12–15], enabling detection of a signature of biological change occurring at the molecular level [16–18]. The use of MBs targeted to vascular endothelial cells via ligand-receptor pairing can be used as a promising tool in the study of angiogenesis. In particular, vascular endothelial growth factor receptor (VEGFR2) and integrin $\alpha_v \beta_3$, which specifically localize in the neovasculature of active tumors, provide a pathway to molecular imaging enabling evaluation of tumor progression [13,19–21]. Molecular imaging is also important for monitoring therapy response and can have a positive impact on therapy design and drug development. Because treatment and drug efficacy can be evaluated earlier by analyzing the molecular signature of disease, USMI may help to accelerate drug development [22,23].

Both ULM and USMI aim to provide enhanced indicators of the disease state, but these techniques have traditionally been performed independently. However, it may be desirable to perform co-localization between the super-resolved vessels and molecular markers to provide simultaneous anatomic and biological information for better disease evaluation. In the case of tumor imaging, super-resolution imaging of the microvasculature could improve tumor localization and visualization of the vasculature, while molecular targeting

could be used to evaluate tumor aggression [24]. By considering anatomic information and molecular information as independent indications of disease, the combination of analyses of each may be used to improve either sensitivity or specificity. In addition, co-localization of these two signals can allow for better association of super resolution anatomic features to the molecular imaging signal. It may also help to determine whether disease-associated anatomic features found via super resolution imaging (e.g. microvascular structures associated with cancer [25–27]) manifest before or after the presence of a disease-associated molecular signal. Conceivably, disease manifestation determined via both super resolution anatomic imaging and super resolution USMI involves information redundancy.

In this paper, we present a new imaging technology: targeted molecular localization (TML), which provides super resolution imaging of vasculature co-localized with the molecular tracer signal. To this end, in the first step of TML imaging, the ULM technique was utilized to resolve microvasculature at super resolution. Singular value decomposition (SVD) was used to remove tissue clutter signals for extraction of circulating MB signals [2,28,29]. In the second step of TML imaging, the targeted MBs were detected and localized, over several consecutive burst trials, as discrete attachment sites. The super resolution microvascular and molecular imaging signals were processed together to generate a TML image.

In this feasibility study, TML images were acquired in a murine tumor model before and after sunitinib anti-vascular treatment. Quantitative measures for vessel index (VI) and molecular index (MI_{TML}) were calculated, in addition to a new metric unique to the TML technique, indicating the ratio of targeted molecular signature to vessel surface (MVR).

3. Materials and Methods

3.1. Microbubble fabrication

Laboratory-made lipid-shelled biotinylated MBs were prepared. By sonicating decafluorobutane gas (F2 Chemicals, Lancashire, UK) with a lipid micellar mixture of polyethylene glycol stearate (Stepan Kessco, Elwood, IL, USA), distearoyl phosphatidylcholine (Avanti Polar Lipids, Alabaster, AL, USA) and biotin-PEG3400-distearoylphosphatidylethanolamine (biotin-PEG-DSPE, Laysan Bio, Arab, AL, USA) in saline, biotinylated MBs were fabricated. VEGFR2-targeted MBs were prepared by conjugating biotinylated anti-mouse VEGFR2 antibody (clone Avas 12a1, eBioscience, San Diego, CA, USA) to the bubbles using a streptavidin linker [30–32].

3.2. Animal preparation

All animal experiments performed in this study were approved by the Institutional Animal Care and Use Committee. A murine hindlimb tumor model was used. C57BL/6 female mice (n = 6) were injected subcutaneously with murine colon adenocarcinoma cells (MC38, 1×10^6 cells, Kerafast, Boston, MA, USA) in the right hindlimb. Imaging was performed 10–14 days after MC38 cell injection, when the implanted tumor had grown to a size of approximately 1 cm. Before imaging, mice were anesthetized with 2% isoflurane gas (Henry Schein, Dublin, OH, USA). A tail vein catheter was placed and mice were then transferred to a heated motion stage (TM150, Indus Instruments, Webster, TX, USA). Mice

were maintained under anesthesia (inhalation of 0.5~1% isoflurane in air) throughout the imaging procedure. The legs were depilated prior to imaging. MBs were administered via the tail vein using a syringe pump (PHD ULTRA, Harvard Apparatus, Holliston, MA, USA).

Mice were imaged before and after anti-angiogenic treatment. Sunitinib is a clinically approved small-molecule pharmacological agent with anti-angiogenic and anti-tumor effects. It is a multi-targeted receptor tyrosine kinase inhibitor that inhibits growth factor receptors such as VEGF receptors and platelet-derived growth factor (PDGF) receptors [33–35]. Sunitinib malate (Selleckchem, Houston, TX) was administered via oral gavage (50 mg/kg body weight) daily for 7 days [33–35]. At the 7-day mark, tumor and control legs were imaged again.

3.3. Targeted molecular localization (TML) imaging approach

Experiments were performed using a Verasonics Vantage system (Verasonics Inc., Kirkland, WA, USA) equipped with an L12–5 (192-element) linear array transducer. The central 128 elements were used both for transmit and receive. A plane wave compounding (PWC) strategy was adopted to obtain the super resolution vasculature map. Plane waves with 9 inclination angles between −4° and 4° with a step of 1° were transmitted at a pulse repetition frequency of 1 kHz to obtain coherently compounded images at a frame rate of 111 Hz. For each angle, a two-cycle pulse was transmitted at 7.8 MHz. A bolus of non-targeted MBs (5×10^7 biotinylated MBs diluted in 50 μL sterile saline) was injected to the mice at a flow rate of 15 μL/min followed by a 50 μL saline flush. The data acquisition started 3–5 min after the start of injection, when the tumor was fully perfused with MBs. A total of 2000 compounded image frames were acquired over a duration of 20 s.

Next, a co-localized sequence was performed to implement our TML approach. This imaging sequence employed 22 virtual sources [36] with a synthetic aperture of 128 elements, a focus of −35 mm, and an effective pitch of 600 μm for coherent compounding. For each virtual source, a pulse inversion (PI) technique [37] was implemented to further improve the imaging sensitivity to MBs [38] (Fig. 1). The imaging pulses (two-cycle duration) were transmitted at a frequency of 5.7 MHz and with MI = 0.12 [38,39].

Differential targeted enhancement (dTE) imaging was performed to extract the USMI signal [38,40–42]. MBs were imaged after a short wait time (6 min) to allow injected MBs to bind to the tumor vessel walls without acoustic interference. High intensity destruction pulses were administered to destroy MBs in the field of view. Pre-burst images were used to measure the late enhancement signals from adherent and circulating MBs. Post-burst images were used to measure only the circulating MB signals. The difference image between the pre- and post-burst signals revealed the signal intensity associated with only adherent MBs.

As Figure. 2 illustrates, VEGFR2-targeted MBs (total of 1×10^7 MBs diluted in 60 μL sterile saline; flow rate of 15 μL/min) were administered successively at three time points ($[t_1, t_1+1.5\text{ min}]$, $[t_2, t_2+1.5\text{ min}]$ and $[t_3, t_3+1\text{ min}]$; 3.3×10^6 MBs for each time point). Following the last infusion, a 50 μL saline flush was administered. For each injection, a 6-minute waiting period was employed between injection and the start of imaging. Next, the imaging sequence was turned on to capture the pre-destruction images. Subsequently, high

intensity acoustic pulses (MI = 0.36, two-cycle duration, center frequency = 5.7 MHz) were transmitted to destroy all MBs in the field of view. The imaging sequence was applied for 2 minutes to acquire both the pre-burst and post-burst PI images.

3.4. TML data processing

Motion correction was performed in order to increase the accuracy of subsequent MBs localization processing steps. In our hindlimb tumor model, respiration caused predominantly rigid motion between frames. This motion was estimated and corrected by applying a 2-D phase-correlation-based rigid geometric image registration method (the 'imregcorr.m' function in MATLAB) [4] to different frames with reference to the first frame of PWC sequence. In the first processing step to constitute the SR anatomical image, singular value decomposition (SVD) was performed on PWC data to extract free moving MBs signals (Fig. 3B to Fig. 3C)). SVD separated the different features of tissue, noise, and moving MBs signals in terms of spatiotemporal coherence. MBs signals exhibited lower spatiotemporal coherence, which were preserved in higher order singular values [2]. Normalized correlation coefficients were calculated by comparing moving MBs images to the point spread function (PSF) of the system according to the amplitude and shape. By setting a threshold (0.8) to correlation coefficients, noise signals and overlapping MB signals were rejected. The approximate positions of separate MBs in each individual frame were then identified as the multiple ROIs on the image (Fig. 3D). For every ROI, intensity-weighted centroid finding in a fine grid (25 μm × 25 μm) was used to localize the positions of all MBs (Fig. 3E) [7,43]. Center positions of MBs from all frames were accumulated to create an image of the tumor vasculature (Fig. 3F).

In the second processing step, targeted molecular localization was performed as follows: mean intensity values were calculated through "slow time" on the pre- and post-burst data, to remove noise signals and residual signals from free moving MBs. Next, subtraction between mean pre-burst and post-burst frames was used to obtain a dTE image of adherent MB signals (Figs. 4A-C). An optimized threshold value was applied to the dTE image as a pre-processing step for extraction and localization of estimated adherent MBs signal. To determine the value of this threshold, a range was first estimated based on the mean normalized signal intensity profile of the ROI (2 mm × 2 mm located at center of tumor or leg) over the pre-burst and post-burst time course. The threshold value for best filtering performance was determined by evaluating the inter-frame area differences of the dTE images with increasing threshold values. The selected threshold value was the value that resulted in maximum area difference, allowing maximal dTE signal immediately above the background. The approximate positions of detected adherent MBs (Fig. 4D) were determined by performing PSF correlation on the thresholded and interpolated dTE image.

To perform the SR co-localization processing, a weight matrix (Fig. 4G) with same dimensions as the SR image was calculated using Equation (1).

$$w_{weight} = \begin{cases} 0, & d > 0.3\ mm \\ e^{-2*d}, & d \leq 0.3\ mm, \end{cases} \quad (1)$$

where d was the distance value of corresponding pixel to the closest vessel referring to the SR image. For each targeting site ROI (e.g. Fig. 4H and Fig. 4I, 0.3 mm * 0.3 mm centered on the initial position), the precise targeting localization was determined by weighted centroid finding (indicated by green crossing in Fig. 4J). Precise targeting sites were localized for each burst trial (Fig. 4E). The TML image was obtained by accumulating all positions of targeting sites from three burst trials and marking these positions with green solid circles with visualization that overlay the super resolution anatomical image color mapped in red (Fig. 4F). Note that the size associated with the circles, intended to enhance visualization, does not impact quantification of the signals. dTE images from three burst trials were also shown overlaid onto the SR image for side by side comparison against the proposed technique.

3.5. Data analysis

During each burst trial, the MB intensity profiles were measured as the mean intensity value within a region of interest (ROI: 2 mm × 2 mm located at center of tumor or tissue) on the PI image. The intensity profiles from the independent trials (n = 6) were normalized, averaged, and reported as mean ± standard deviation (SD) over multiple burst trials. MB intensity before and after the burst was then tested for a statistically significant difference.

B-mode images, SR images superimposed with dTE, and TML images were shown for control leg, tumor and tumor with sunitinib. The diameters of selected vessels in SR images were determined by full-width at half-maximum measurements perpendicular to the axis of the detected vessels.

The intra-tumoral space and intra-tissue (control leg) space were manually segmented for each case by one of the authors (FZ) (Fig. 5). Within the selected regions, vascular density was quantified as vessel index (VI), defined as the pixel number containing super-resolution blood vessel signals divided by the total pixel number of the ROI. In the same ROI, molecular index (MI_{TML}) was calculated as the number of effective localized targeting sites divided by the total pixel number. An indicator MVR was used to evaluate evolving vasculature disease as a ratio of vessels with targeted molecules, calculated as:

$$\mathrm{MVR} = \frac{\mathrm{MI}_{TML}}{\mathrm{VI}} \times 100\% \quad (2)$$

A comparison between the control leg, tumor and tumor with sunitinib treatment was performed on VI, MI_{TML} and MVR values, respectively. All the statistical significance was determined by a one-way analysis of variance (ANOVA) and *post hoc* multiple comparisons. A P-value < .05 was considered to indicate a statistically significant difference.

4. Results

The measured MB intensity curves (mean ± SD) in Figure 6 show the changes in MBs signal intensity after administration of high intensity destruction pulses in different burst trials for different groups. The difference between pre-burst and post-burst indicates the adherent MB intensity values. In profiles for the control leg and tumor with sunitinib, no

significant differences ($p > 0.5$, $n = 6$) are found between pre-burst and post-burst MB signal intensity, while for the tumor, the pre-burst signal intensities are significantly higher than the post-burst signal intensities ($p < 0.0005$, $n = 6$) in all the three burst trials. This indicates that the control leg and sunitinib-treated tumor groups have fewer targeted MBs than the untreated tumor group.

The B-mode images, dTE images, and TML images corresponding to different groups from two representative cases are shown in Figure 7 and Figure 8, respectively. The full microvasculature mapping is color mapped in red, where the saturation represents the count of detected MBs events. The adherent MB signals targeting sites onto the vessels are shown as green dots. In conventional B mode images, it is difficult to identify the vessels in either the control leg or tumor groups. Using the super resolution technique, the fine scale vasculature is shown for all groups. The SR with dTE overlaying images of the tumors show the co-localization results of the detected adherent MBs signals to the separate vessel. The adherent MBs targeting sites are defined in TML images and correlate to the microvessels for all groups by using the TML technique. The qualitative results show much less binding from targeted MBs in the healthy tissue (leg) and tumors with sunitinib treatment, compared to those in tumor (no sunitinib), which is consistent with the quantitative adherent MBs intensity profiles result (Fig. 6).

The diameters of both the leg and tumor vessels obtained by super resolution processing were quantified as measurements of FWHM values. 72 vessels were manually extracted from the control leg and 144 vessels from the tumor. Cross-sections of several vessel profiles, indicated by lines 1 to 3 in Figure 9A, are shown in Figures 9C to 9E. The branched vessels are identified in Figure 9E. A histogram graph in Figure 9B shows that control leg vessels have diameters in the range of 50–200 μm and tumor vessels have diameters in range of 25–150 μm. A summary of the vessel diameters values is shown in Table 1.

The quantitative VI, MI_{TML} and MVR values are shown in Figure 10. The mean ± s.d. for VI is 26% ± 8% for control tissue (leg), 37% ± 7% for tumor, and 36% ± 9% for tumor with sunitinib (Fig. 10A). For MI_{TML}, these values are 0.03% ± 0.02% for control tissue, 0.08% ± 0.03% for tumor, and 0.01% ± 0.01% for tumor with drug (Fig. 10B, left). The mean ± s.d. for MVR is 0.1% ± 0.08% for control tissue, 0.23% ± 0.1% for tumor, and 0.03% ± 0.02% for tumor with sunitinib (Fig. 10B, right). Comparing control tissue results with hindlimb tumor results, the smaller VI and MI_{TML} are observed, demonstrating that normal mouse leg tissue has lower vascular density and less MB adhesion than mouse hindlimb tumors. Comparing tumors treated with sunitinib to those without treatment, lower MI_{TML} while comparable VI values are found. Comparing control tissue to tumor with drug treatment, VI is decreased while MI_{TML} is increased. MVR values show that the concentration of targeted molecules on detected vessels is lower in the control tissue and sunitinib-treated tumor compared to that in the untreated tumor.

Statistical significance was determined for these quantitative values associated with the different groups. The results reveal statistically significant differences between control tissue and tumor for VI ($p < 0.05$), between control tissue and tumor for MI_{TML} ($p < 0.005$), and between tumor without and with sunitinib for MI_{TML} ($p < 0.0005$). Statistically significant

differences in MVR are shown between the control leg and tumor ($p < 0.05$), between tumors with and without sunitinib treatment ($p < 0.001$), and between control legs and tumors with sunitinib ($p < 0.05$).

5. Discussion

In this study, a new targeted molecular localization (TML) technique was developed to combine super resolution vascular imaging with the distribution of vascular disease markers as detected by molecularly targeted MBs. In this way, co-localized anatomic and biological information was provided. This method was applied to a murine model in experimental control group, untreated hindlimb tumor group, and tumor post-treatment with sunitinib. A new quantitative parameter, MVR, was validated to uniquely, among the three parameters evaluated in this study, differentiate between these models based on the ratio between molecular marker coverage and density of super-resolution vessel signal.

Previous studies have demonstrated similar techniques to produce high-resolution images (150~200 μm) of vasculature overlaid with ultrasound molecular imaging (USMI) signals using the “transmit low/receive high” dual-transducer approach [44]. However, unique to our developed TML technique in this study is a co-localization between the detected adherent MBs and the microvasculature mappings (Figs. 7 and 8). A super resolution vascular map was obtained by accumulating 2000 frames. This vascular map provided a reference for adherent MB detection from the dTE image, which as a differential measurement is susceptible to high levels of noise. By determining the most probable USMI signal locations using the associated super resolution image, the dTE signal was constrained to regions overlapping with microvasculature for the purpose of specifically localizing regions of the microvascular containing molecular markers. The co-localization of super resolution and USMI signals provides an opportunity to analyze unique information related to the proportion of microvasculature containing molecular markers. This measurement of coverage ratio for vessels with VEGFR2-targeted MBs (MVR) was demonstrated to distinguish all study groups, with and without treatment versus the control group (Fig. 10).

Using the proposed TML technique, the response to drug in terms of both the vascularity and detectable molecular signature in tumor, are demonstrated (Fig. 10). This new approach presents opportunities for analyzing relationships or time courses of microvascular anatomy and vascular molecular targets. In the literature, it has been reported that USMI detects alterations of biological change occurring at the molecular level in response to disease much earlier than conventional diagnostic methods [18,45,46]. Therefore, USMI has the potential to provide powerful predictive information in the earliest stages of disease. Targeted/molecular imaging techniques have been applied to various applications including angiography and measurement of therapeutic response [47–49]. Referring to results obtained in this study, when comparing the treated and untreated tumor groups, super resolution images revealed no significant difference based on vascular index (VI). However, the molecular index (MI_{TML}) demonstrated a significant difference between the treated and untreated groups (Fig. 10). This result validates the observation that changes in vascular endothelial markers to anti-angiogenic drugs precede a change in vascular architecture.

The SR approach yielded spatial resolution down to 28.8 μm (Fig. 9 and Table 1), which was similar to the selected interpolation grid size (25 μm × 25 μm). Resolution could be improved to a capillary level (< 10 μm) by detecting MBs using a smaller interpolation grid to further improve our TML technique. However, longer acquisition time and greater number of MBs events would be required [2,50]. Nevertheless, the current resolution achieved in this study provided greater than ten-fold resolution improvement compared to traditional ultrasound imaging (200 μm~1 mm), which is broadly consistent with previous examples of super-resolution imaging [10].

An exponential weighing function was chosen in this study. Other functions in which weights are inversely related to distance may also be used. This selection only impacts the visualization of the TML images but not the estimated number of targeting sites of the detected adherent MBs and the resultant quantitative results. The cut-off distance value for calculation of the weighting matrix, and the chosen ROI size, for precise localization was determined by the −6 dB resolution of dTE imaging sequence. This approach attempts to properly retain the dTE signals of individual MBs.

In this study, the TML technique co-localized the adherent MBs signals with SR signal, and visualizations were presented where the adherence MBs signals were displayed as discrete points overlaid on top of underlying super-resolved images of the vascular network. Although represented as discrete points, as with the super-resolution technique more generally, it is likely that more than one MB is present within each dTE resolution cell. The localization of adherent MB sites in the TML technique will more faithfully represent single MB sites with lower MBs injection concentrations and less bursting events per frame. Nevertheless, as a technical feasibility study, the proposed method attempted to resolve the individual MB providing a pathway towards super resolution molecular imaging and as a pre-processing step for quantification (i.e. the MVR parameter). Additionally, while the TML image visualization technique demonstrated in this study conveys precise localization of adherent MB signal, an alternative approach may involve weighting dTE image by Equation 1 where dTE signal is co-localized with SR signals but without displays as point localizations.

In the implementation of TML selected for this feasibility study, one limitation is that two separate injections were utilized: a high dose (5×10^7) non-targeted and a relatively low dose (1×10^7) VEGFR2-targeted MB administration. A higher dose non-targeted MBs injection ensured enough MB events to detect for super resolution imaging and potentially shortened the acquisition time to obtain the full microvasculature mapping [51]. For molecular imaging, static adherent MBs were extracted based on their dTE intensity and a relatively low dose was selected to identify targeting of discrete MBs. During the entire imaging procedure, the mice were anesthetized and physically immobile. Similarly, the transducer was mounted in a fixture to avoid inter-frame motion. Ideally, a single injection and one dataset will be used in any future clinical translation of this technique. This will simplify the procedure and reduce the impact of inter-frame motion in MBs localization [52]. We hypothesize that it may be possible to use a low dose targeted MBs injection to simultaneously bind to tumor endothelial cells and act as a vascular tracer for super-resolution imaging of the tumor microvasculature. In the low dose case, it would be necessary to track MBs through time and

plot their trajectories to reconstruct the full microvascular mapping. Tracking MBs can be achieved by pairing all the MBs in frame N to N+1 based on the minimum distance principle [2,4] in high frame rate. A single-injection TML imaging strategy design requires a careful balance between the frame rate and imaging sensitivity to MBs and is beyond the scope of the current paper.

6. Conclusion

In this study, a new targeted molecular localization (TML) technique was developed to co-localize super resolution microvessels imaging with VEGFR2-targeted MBs detection, thus providing combined anatomical and biological information at a fine vascular scale. The results have demonstrated the feasibility of the proposed method for evaluating evolving vascular disease with significant differences ($P < 0.05$) found between three disease models that included tumor (no drug therapy), tumor with drug therapy and control tissue (leg). We were able to validate the precedent vascular molecular targets changes in response to sunitinib compared to the microvascular anatomy. The co-localization could be a useful to differentiate the character and evolution of regional vascular structure and molecular information in potential applications such as cancer and vascular disease.

Sources of funding:

this study was supported by the NHLBI of National Institutes of Health under award number R01-HL132395 and R01-EB023055.

Reference:

1. Christensen-Jeffries K, Couture O, Dayton PA, et al. Super-resolution Ultrasound Imaging. Ultrasound Med Biol. 2020;46(4):865–891. doi:10.1016/j.ultrasmedbio.2019.11.013 [PubMed: 31973952]
2. Errico C, Pierre J, Pezet S, et al. Ultrafast ultrasound localization microscopy for deep super-resolution vascular imaging. Nature. 2015;527(7579):499–502. doi:10.1038/nature16066 [PubMed: 26607546]
3. Couture O, Hingot V, Heiles B, et al. Ultrasound Localization Microscopy and Super-Resolution: A State of the Art. IEEE Trans Ultrason Ferroelectr Freq Control. 2018;65(8):1304–1320. doi:10.1109/TUFFC.2018.2850811 [PubMed: 29994673]
4. Song P, Trzasko JD, Manduca A, et al. Improved Super-Resolution Ultrasound Microvessel Imaging With Spatiotemporal Nonlocal Means Filtering and Bipartite Graph-Based Microbubble Tracking. IEEE Trans Ultrason Ferroelectr Freq Control. 2018;65(2):149–167. doi:10.1109/TUFFC.2017.2778941 [PubMed: 29389649]
5. Zhu J, Lin S, Leow CH, et al. High Frame Rate Contrast-Enhanced Ultrasound Imaging for Slow Lymphatic Flow: Influence of Ultrasound Pressure and Flow Rate on Bubble Disruption and Image Persistence. Ultrasound Med Biol. 2019;45(9):2456–2470. doi:10.1016/j.ultrasmedbio.2019.05.016 [PubMed: 31279503]
6. Siepmann M, Schmitz G, Bzyl J, et al. Imaging tumor vascularity by tracing single microbubbles. In: 2011 IEEE International Ultrasonics Symposium. IEEE; 2011:1906–1909. doi:10.1109/ULTSYM.2011.0476
7. Zhu J, Rowland EM, Harput S, et al. 3D Super-Resolution US Imaging of Rabbit Lymph Node Vasculature in Vivo by Using Microbubbles. Radiology. 2019;291(3):642–650. doi:10.1148/radiol.2019182593 [PubMed: 30990382]
8. Demené C, Tiran E, Sieu L-A, et al. 4D microvascular imaging based on ultrafast Doppler tomography. Neuroimage. 2016;127:472–483. [PubMed: 26555279]

9. Kanoulas E, Butler M, Rowley C, et al. Super-Resolution Contrast-Enhanced Ultrasound Methodology for the Identification of In Vivo Vascular Dynamics in 2D: Invest Radiol. 2019;54(8):500–516. doi:10.1097/RLI.0000000000000565 [PubMed: 31058661]
10. Lin F, Shelton SE, Espíndola D, et al. 3-D Ultrasound Localization Microscopy for Identifying Microvascular Morphology Features of Tumor Angiogenesis at a Resolution Beyond the Diffraction Limit of Conventional Ultrasound. Theranostics. 2017;7(1):196–204. doi:10.7150/thno.16899 [PubMed: 28042327]
11. Lowerison MR, Huang C, Lucien F, et al. Ultrasound localization microscopy of renal tumor xenografts in chicken embryo is correlated to hypoxia. Sci Rep. 2020;10(1). doi:10.1038/s41598-020-59338-z
12. Wright WH, McCreery TP, Krupinski EA, et al. Evaluation of new thrombus-specific ultrasound contrast agent. Acad Radiol. 1998;5:S240–S242. doi:10.1016/S1076-6332(98)80117-7 [PubMed: 9561090]
13. Ellegala DB, Leong-Poi H, Carpenter JE, et al. Imaging Tumor Angiogenesis With Contrast Ultrasound and Microbubbles Targeted to α v β 3. Circulation. 2003;108(3):336–341. doi:10.1161/01.CIR.0000080326.15367.0C [PubMed: 12835208]
14. Kaufmann BA, Sanders JM, Davis C, et al. Molecular Imaging of Inflammation in Atherosclerosis With Targeted Ultrasound Detection of Vascular Cell Adhesion Molecule-1. Circulation. 2007;116(3):276–284. doi:10.1161/CIRCULATIONAHA.106.684738 [PubMed: 17592078]
15. Lindner JR, Song J, Christiansen J, et al. Ultrasound Assessment of Inflammation and Renal Tissue Injury With Microbubbles Targeted to P-Selectin. Circulation. 2001;104(17):2107–2112. doi:10.1161/hc4201.097061 [PubMed: 11673354]
16. Bachawal SV, Jensen KC, Lutz AM, et al. Earlier Detection of Breast Cancer with Ultrasound Molecular Imaging in a Transgenic Mouse Model. Cancer Res. 2013;73(6):1689–1698. doi:10.1158/0008-5472.CAN-12-3391 [PubMed: 23328585]
17. Kaufmann BA, Carr CL, Belcik JT, et al. Molecular Imaging of the Initial Inflammatory Response in Atherosclerosis: Implications for Early Detection of Disease. Arterioscler Thromb Vasc Biol. 2010;30(1):54–59. doi:10.1161/ATVBAHA.109.196386 [PubMed: 19834105]
18. Wang S, Unnikrishnan S, Herbst EB, et al. Ultrasound Molecular Imaging of Inflammation in Mouse Abdominal Aorta: Invest Radiol. 2017;52(9):499–506. doi:10.1097/RLI.0000000000000373
19. Tardy I, Pochon S, Theraulaz M, et al. Ultrasound Molecular Imaging of VEGFR2 in a Rat Prostate Tumor Model Using BR55. Invest Radiol. 2010;45(10):573–578. doi:10.1097/RLI.0b013e3181ee8b83 [PubMed: 20808233]
20. Pysz MA, Machtaler SB, Seeley ES, et al. Vascular Endothelial Growth Factor Receptor Type 2–targeted Contrast-enhanced US of Pancreatic Cancer Neovasculature in a Genetically Engineered Mouse Model: Potential for Earlier Detection. Radiology. 2015;274(3):790–799. doi:10.1148/radiol.14140568 [PubMed: 25322341]
21. McMahon G. VEGF Receptor Signaling in Tumor Angiogenesis. The Oncologist. 2000;5(S1):3–10. doi:10.1634/theoncologist.5-suppl_1-3 [PubMed: 10804084]
22. Weber WA, Czernin J, Phelps ME, et al. Technology Insight: novel imaging of molecular targets is an emerging area crucial to the development of targeted drugs. Nat Clin Pract Oncol. 2008;5(1):44–54. doi:10.1038/ncponc0982 [PubMed: 18097456]
23. Cai W, Rao J, Gambhir SS, et al. How molecular imaging is speeding up antiangiogenic drug development. Mol Cancer Ther. 2006;5(11):2624–2633. doi:10.1158/1535-7163.MCT-06-0395 [PubMed: 17121909]
24. Marchal C, Redondo M, Padilla M, et al. Expression of prostate specific membrane antigen (PSMA) in prostatic adenocarcinoma and prostatic intraepithelial neoplasia. Histol Histopathol. 2004;19:715–718. [PubMed: 15168332]
25. Tong RT, Boucher Y, Kozin SV, et al. Vascular Normalization by Vascular Endothelial Growth Factor Receptor 2 Blockade Induces a Pressure Gradient Across the Vasculature and Improves Drug Penetration in Tumors. Cancer Res. 2004;64(11):3731–3736. doi:10.1158/0008-5472.CAN-04-0074 [PubMed: 15172975]

26. Nagy JA, Dvorak HF. Heterogeneity of the tumor vasculature: the need for new tumor blood vessel type-specific targets. Clin Exp Metastasis. 2012;29(7):657–662. doi:10.1007/s10585-012-9500-6 [PubMed: 22692562]
27. Carmeliet P, Jain RK. Angiogenesis in cancer and other diseases. Nature. 2000;407(6801):249–257. doi:10.1038/35025220 [PubMed: 11001068]
28. Baranger J, Arnal B, Perren F, et al. Adaptive Spatiotemporal SVD Clutter Filtering for Ultrafast Doppler Imaging Using Similarity of Spatial Singular Vectors. IEEE Trans Med Imaging. 2018;37(7):1574–1586. doi:10.1109/TMI.2018.2789499 [PubMed: 29969408]
29. Demene C, Deffieux T, Pernot M, et al. Spatiotemporal Clutter Filtering of Ultrafast Ultrasound Data Highly Increases Doppler and fUltrasound Sensitivity. IEEE Trans Med Imaging. 2015;34(11):2271–2285. doi:10.1109/TMI.2015.2428634 [PubMed: 25955583]
30. Lee DJ, Lyshchik A, Huamani J, et al. Relationship Between Retention of a Vascular Endothelial Growth Factor Receptor 2 (VEGFR2)-Targeted Ultrasonographic Contrast Agent and the Level of VEGFR2 Expression in an In Vivo Breast Cancer Model. J Ultrasound Med. 2008;27(6):855–866. doi:10.7863/jum.2008.27.6.855 [PubMed: 18499845]
31. Willmann JK, Cheng Z, Davis C, et al. Targeted Microbubbles for Imaging Tumor Angiogenesis: Assessment of Whole-Body Biodistribution with Dynamic Micro-PET in Mice. Radiology. 2008;249(1):212–219. doi:10.1148/radiol.2491072050 [PubMed: 18695212]
32. Willmann JK, Lutz AM, Paulmurugan R, et al. Dual-targeted Contrast Agent for US Assessment of Tumor Angiogenesis in Vivo. Radiology. 2008;248(3):936–944. doi:10.1148/radiol.2483072231 [PubMed: 18710985]
33. Chow LQM, Eckhardt SG. Sunitinib: From Rational Design to Clinical Efficacy. J Clin Oncol. 2007;25(7):884–896. doi:10.1200/JCO.2006.06.3602 [PubMed: 17327610]
34. Faivre S, Demetri G, Sargent W, et al. Molecular basis for sunitinib efficacy and future clinical development. Nat Rev Drug Discov. 2007;6(9):734–745. doi:10.1038/nrd2380 [PubMed: 17690708]
35. Rojas JD, Lin F, Chiang Y-C, et al. Ultrasound Molecular Imaging of VEGFR-2 in Clear-Cell Renal Cell Carcinoma Tracks Disease Response to Antiangiogenic and Notch-Inhibition Therapy. Theranostics. 2018;8(1):141–155. doi:10.7150/thno.19658 [PubMed: 29290798]
36. Frazier CH, O'Brien WD. Synthetic aperture techniques with a virtual source element. IEEE Trans Ultrason Ferroelectr Freq Control. 1998;45(1):196–207. doi:10.1109/58.646925 [PubMed: 18244172]
37. Shen C-C, Chou Y-H, Li P-C. Pulse Inversion Techniques in Ultrasonic Nonlinear Imaging. J Med Ultrasound. 2005;13(1):3–17. doi:10.1016/S0929-6441(09)60073-4
38. Herbst EB, Unnikrishnan S, Klibanov AL, et al. Validation of Normalized Singular Spectrum Area as a Classifier for Molecularly Targeted Microbubble Adherence. Ultrasound Med Biol. 2019;45(9):2493–2501. doi:10.1016/j.ultrasmedbio.2019.05.026 [PubMed: 31227262]
39. Herbst EB, Wang S, Klibanov AL, et al. Microbubble signal classification using normalized singular spectrum area based filtering methods. In: 2017 IEEE International Ultrasonics Symposium (IUS). IEEE; 2017:1–3. doi:10.1109/ULTSYM.2017.8091812
40. Ferrara K, Pollard R, Borden M. Ultrasound Microbubble Contrast Agents: Fundamentals and Application to Gene and Drug Delivery. Annu Rev Biomed Eng. 2007;9(1):415–447. doi:10.1146/annurev.bioeng.8.061505.095852 [PubMed: 17651012]
41. Anderson CR, Hu X, Zhang H, et al. Ultrasound Molecular Imaging of Tumor Angiogenesis With an Integrin Targeted Microbubble Contrast Agent: Invest Radiol. 2011;46(4):215–224. doi:10.1097/RLI.0b013e3182034fed [PubMed: 21343825]
42. Wang S, Herbst EB, Mauldin FW, et al. Ultra–Low-Dose Ultrasound Molecular Imaging for the Detection of Angiogenesis in a Mouse Murine Tumor Model: How Little Can We See? Invest Radiol. 2016;51(12):758–766. doi:10.1097/RLI.0000000000000310 [PubMed: 27654582]
43. Song P, Manduca A, Trzasko JD, et al. On the Effects of Spatial Sampling Quantization in Super-Resolution Ultrasound Microvessel Imaging. IEEE Trans Ultrason Ferroelectr Freq Control. 2018;65(12):2264–2276. doi:10.1109/TUFFC.2018.2832600 [PubMed: 29993999]

44. Shelton SE, Lindsey BD, Tsuruta JK, et al. Molecular Acoustic Angiography: A New Technique for High-resolution Superharmonic Ultrasound Molecular Imaging. Ultrasound Med Biol. 2016;42(3):769–781. doi:10.1016/j.ultrasmedbio.2015.10.015 [PubMed: 26678155]
45. Bachawal SV, Jensen KC, Lutz AM, et al. Earlier Detection of Breast Cancer with Ultrasound Molecular Imaging in a Transgenic Mouse Model. Cancer Res. 2013;73(6):1689–1698. doi:10.1158/0008-5472.CAN-12-3391 [PubMed: 23328585]
46. Kaufmann BA, Carr CL, Belcik JT, et al. Molecular Imaging of the Initial Inflammatory Response in Atherosclerosis: Implications for Early Detection of Disease. Arterioscler Thromb Vasc Biol. 2010;30(1):54–59. doi:10.1161/ATVBAHA.109.196386 [PubMed: 19834105]
47. Bam R, Daryaei I, Abou-Elkacem L, et al. Toward the Clinical Development and Validation of a Thy1-Targeted Ultrasound Contrast Agent for the Early Detection of Pancreatic Ductal Adenocarcinoma. Invest Radiol. 2020;Publish Ahead of Print. doi:10.1097/RLI.0000000000000697
48. Helbert A, Von Wronski M, Colevret D, et al. Ultrasound Molecular Imaging With BR55, a Predictive Tool of Antiangiogenic Treatment Efficacy in a Chemo-Induced Mammary Tumor Model. Invest Radiol. 2020;Publish Ahead of Print. doi:10.1097/RLI.0000000000000661
49. Diakova GB, Du Z, Klibanov AL. Targeted Ultrasound Contrast Imaging of Tumor Vasculature With Positively Charged Microbubbles. Invest Radiol. 2020;Publish Ahead of Print. doi:10.1097/RLI.0000000000000699
50. Hingot V, Errico C, Heiles B, et al. Microvascular flow dictates the compromise between spatial resolution and acquisition time in Ultrasound Localization Microscopy. Sci Rep. 2019;9(1). doi:10.1038/s41598-018-38349-x
51. Christensen-Jeffries K, Brown J, Harput S, et al. Poisson Statistical Model of Ultrasound Super-Resolution Imaging Acquisition Time. IEEE Trans Ultrason Ferroelectr Freq Control. 2019;66(7):1246–1254. doi:10.1109/TUFFC.2019.2916603 [PubMed: 31107645]
52. Hingot V, Errico C, Tanter M, et al. Subwavelength motion-correction for ultrafast ultrasound localization microscopy. Ultrasonics. 2017;77:17–21. doi:10.1016/j.ultras.2017.01.008 [PubMed: 28167316]

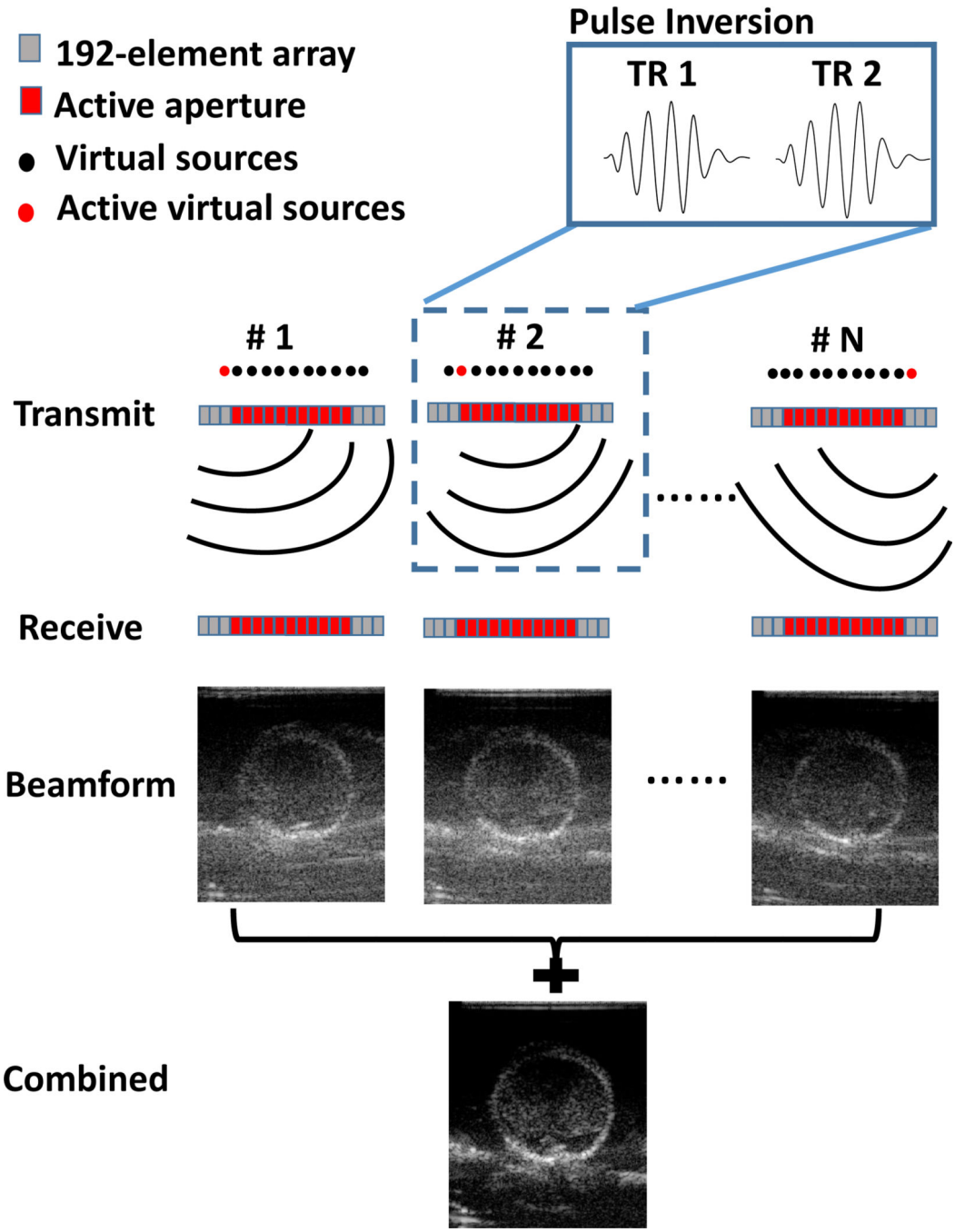

FIGURE 1.

Principle of the multi-virtual sources compounding with pulse inversion imaging sequence. The central 128 elements of 192-element probe were used both for transmit and receive. A single higher contrast image was obtained by compounding 22 (N=22) low contrast images from different transmit-receive events.

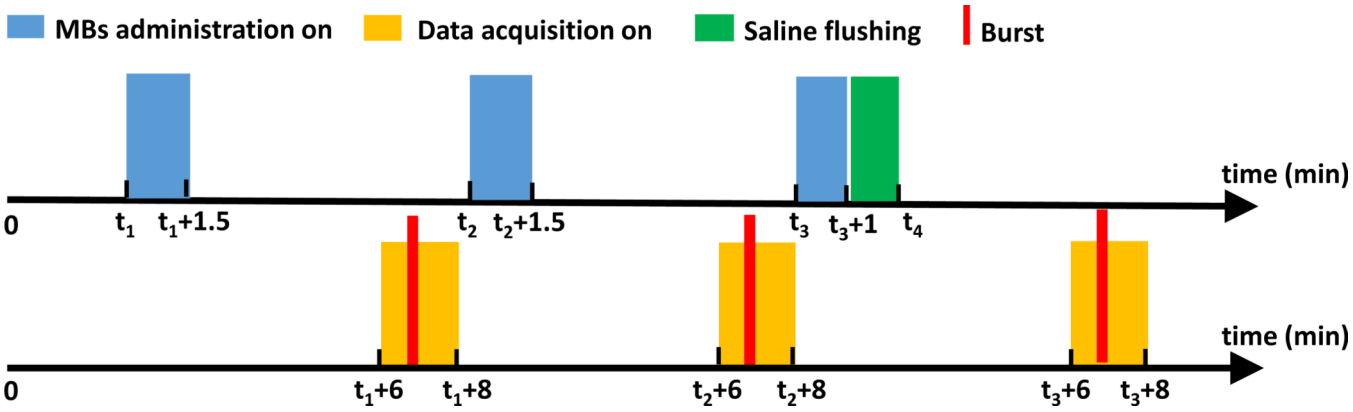

FIGURE 2.
Timeline of imaging sequence for targeted MBs injection and data acquisition.

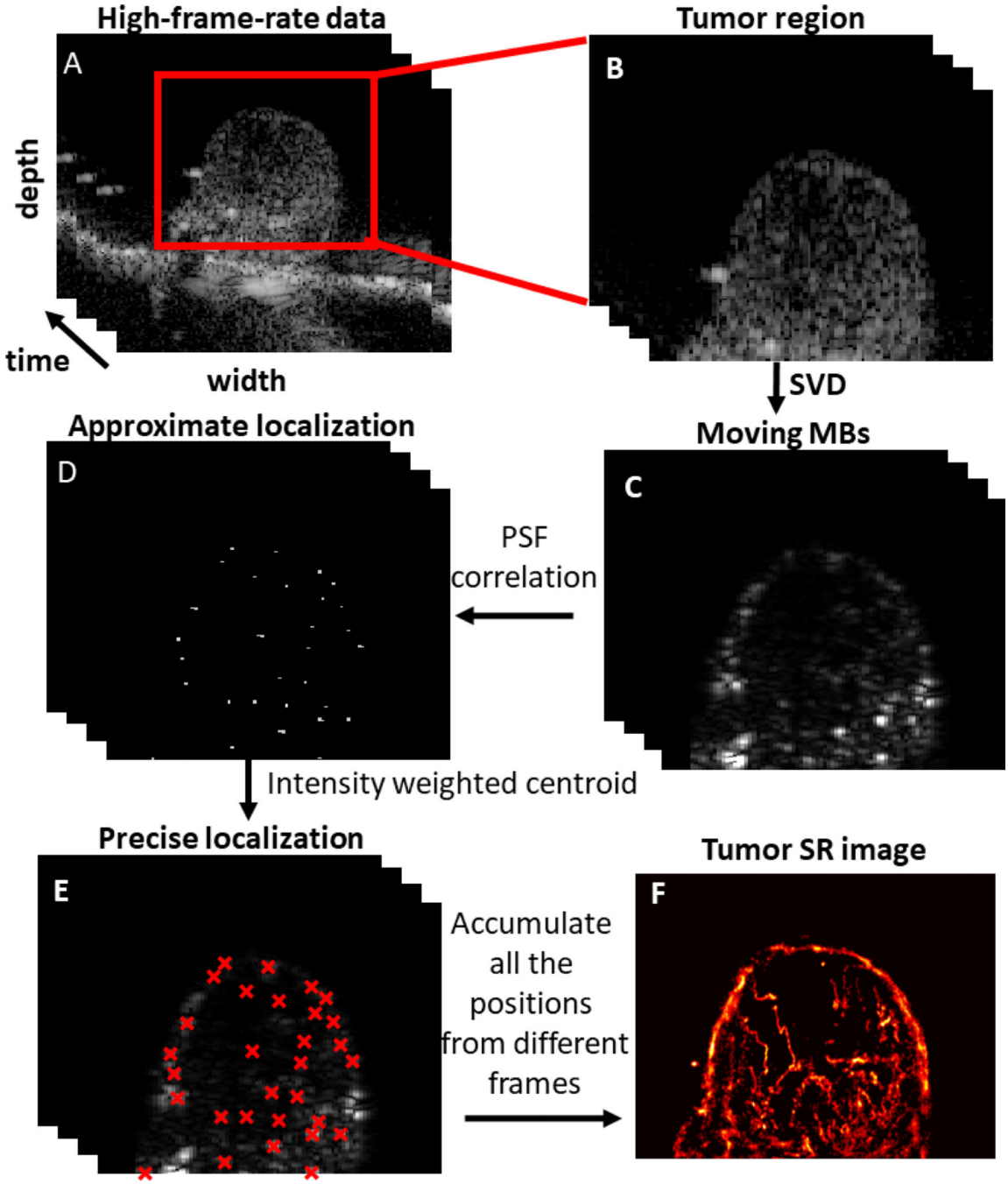

FIGURE 3.

Flowchart of super resolution technique to obtain the microvasculature image. (A) The acquired B-mode image based on PWC. (B) Region of interest containing the tumor. (C) SVD processing was performed to extract the free-moving MBs. The localization of individual MBs was processed with (D) PSF correlation and (E) intensity weighted centroid finding. (F) The positions of detected MBs on thousands of frames were accumulated to constitute a SR image.

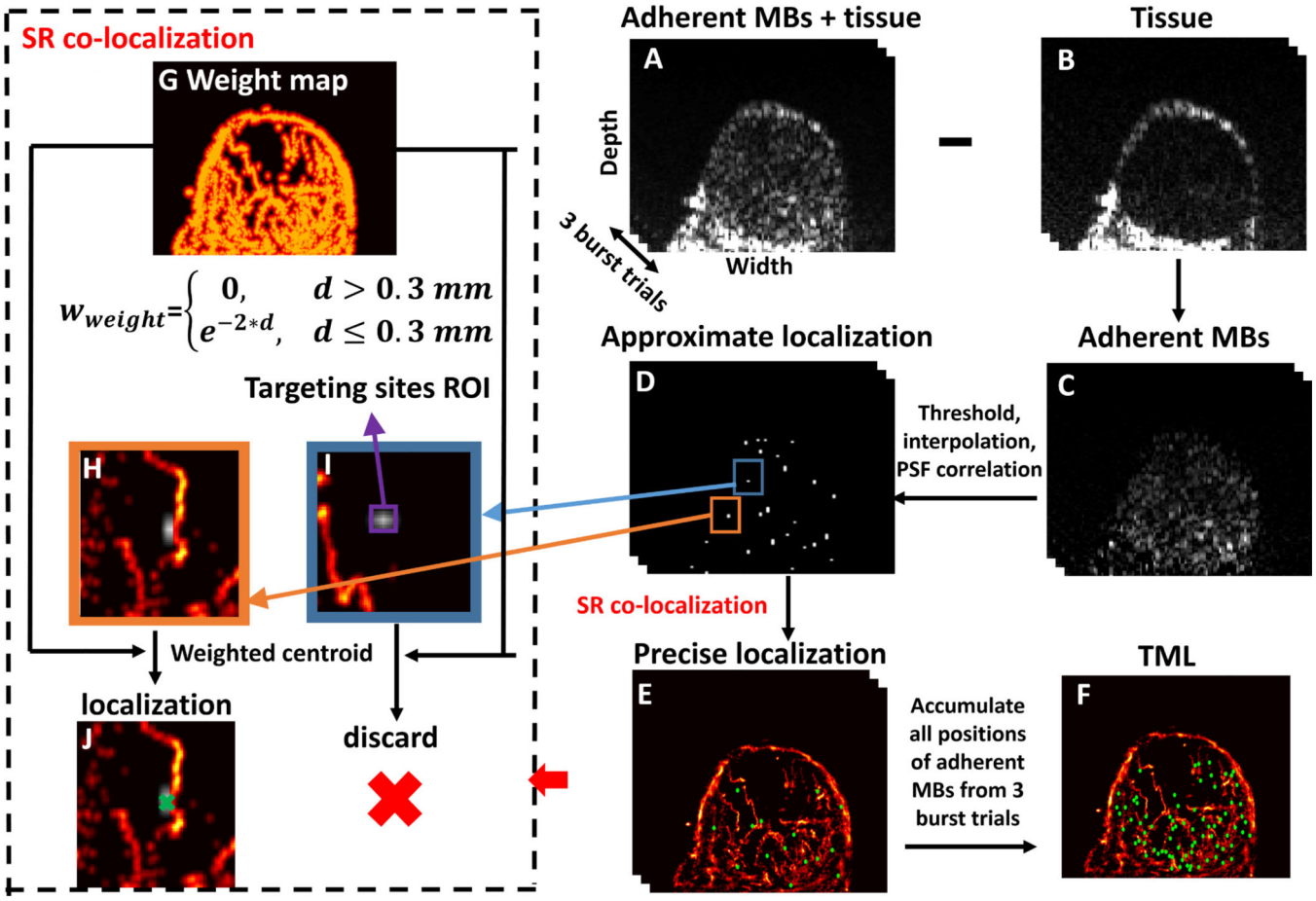

FIGURE 4.

Flowchart of TML technique. PI images of (A) pre-burst representing adherent MBs and tissue and (B) post-burst representing only tissue, (C) dTE images representing adherent MBs, (D) Approximate localization of separate adherent MB by thresholding, interpolation and PSF correlation, (E) Precise targeting sites localization by SR co-localization process for each burst trial, (F) TML image by accumulating all positions of targeting sites from three burst trials. SR co-localization process: a weight map (G) was calculated based on the distance values to the closest vessels referring to the SR image according to Equation (1). For each targeting site, e.g. (H) and (I), the effective identified position indicated by green crossing in (J) was calculated by finding the weighted centroid.

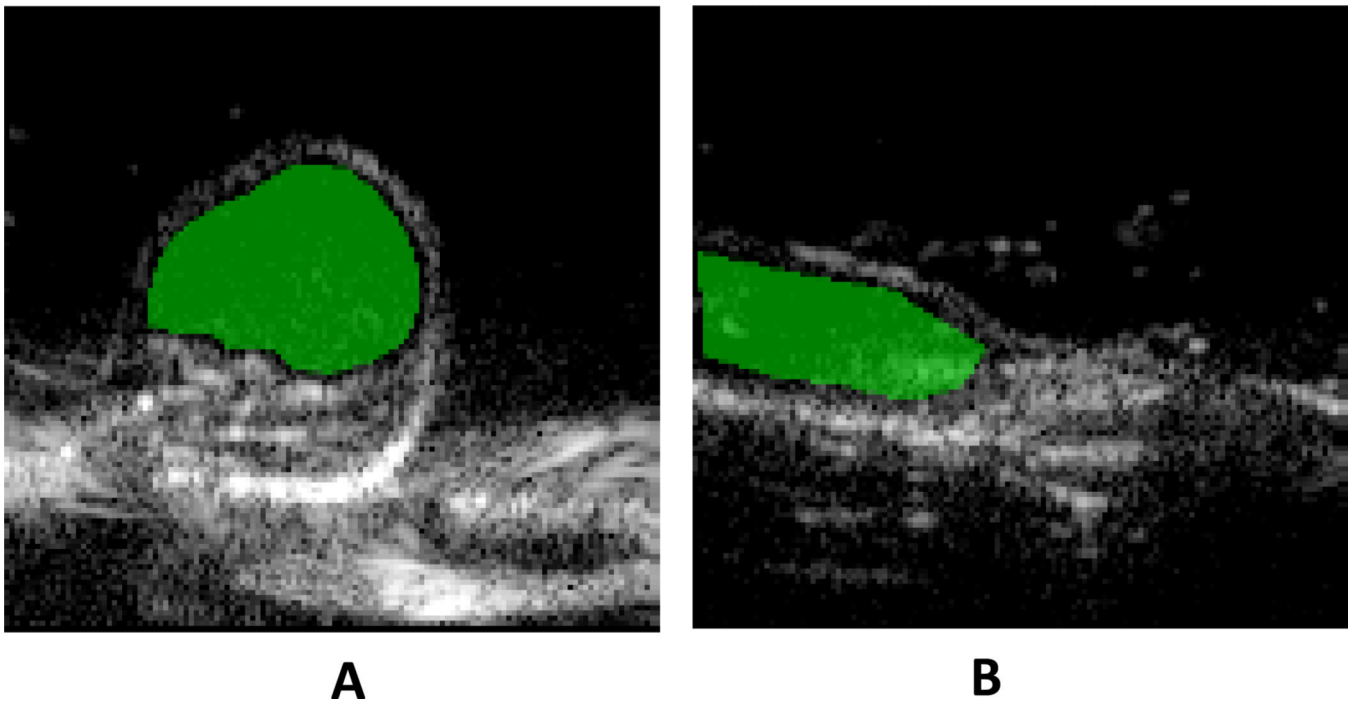

FIGURE 5.

Manually segmented regions of interest for VI and MI_{TML} measurement in (A) tumor and (B) control tissue (leg), respectively.

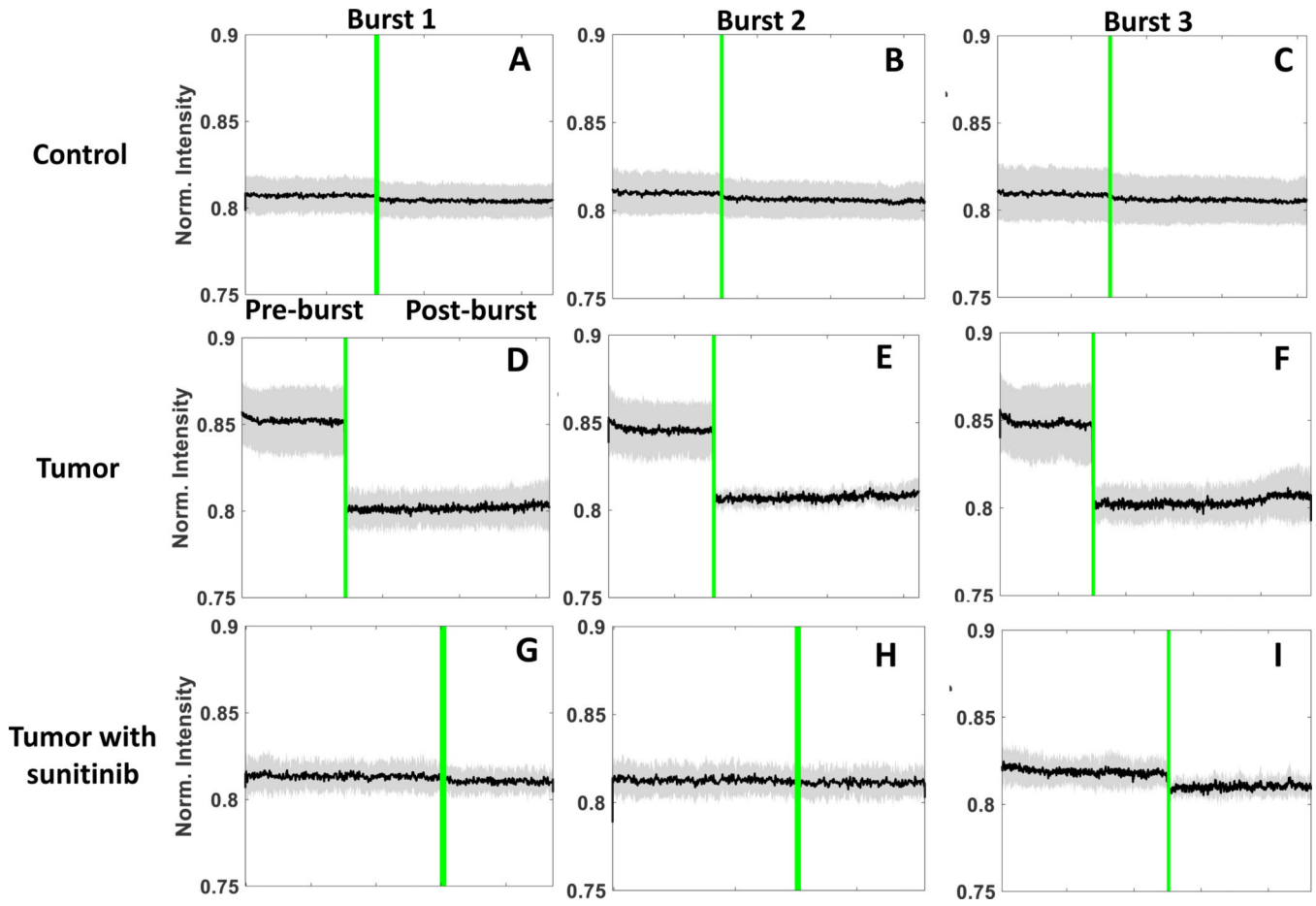

FIGURE 6.

Quantitative adherent MBs intensity profiles of (A-C) control leg, (D-F) tumor and (G-I) tumor with sunitinib over the course of multiple burst trials. In the case of the tumor (middle row), a statistically significant difference in pre- and post-burst signal indicates the presence of adherent MBs (molecular) signal. This difference is not present in control leg (upper row) or tumor with sunitinib (lower row).

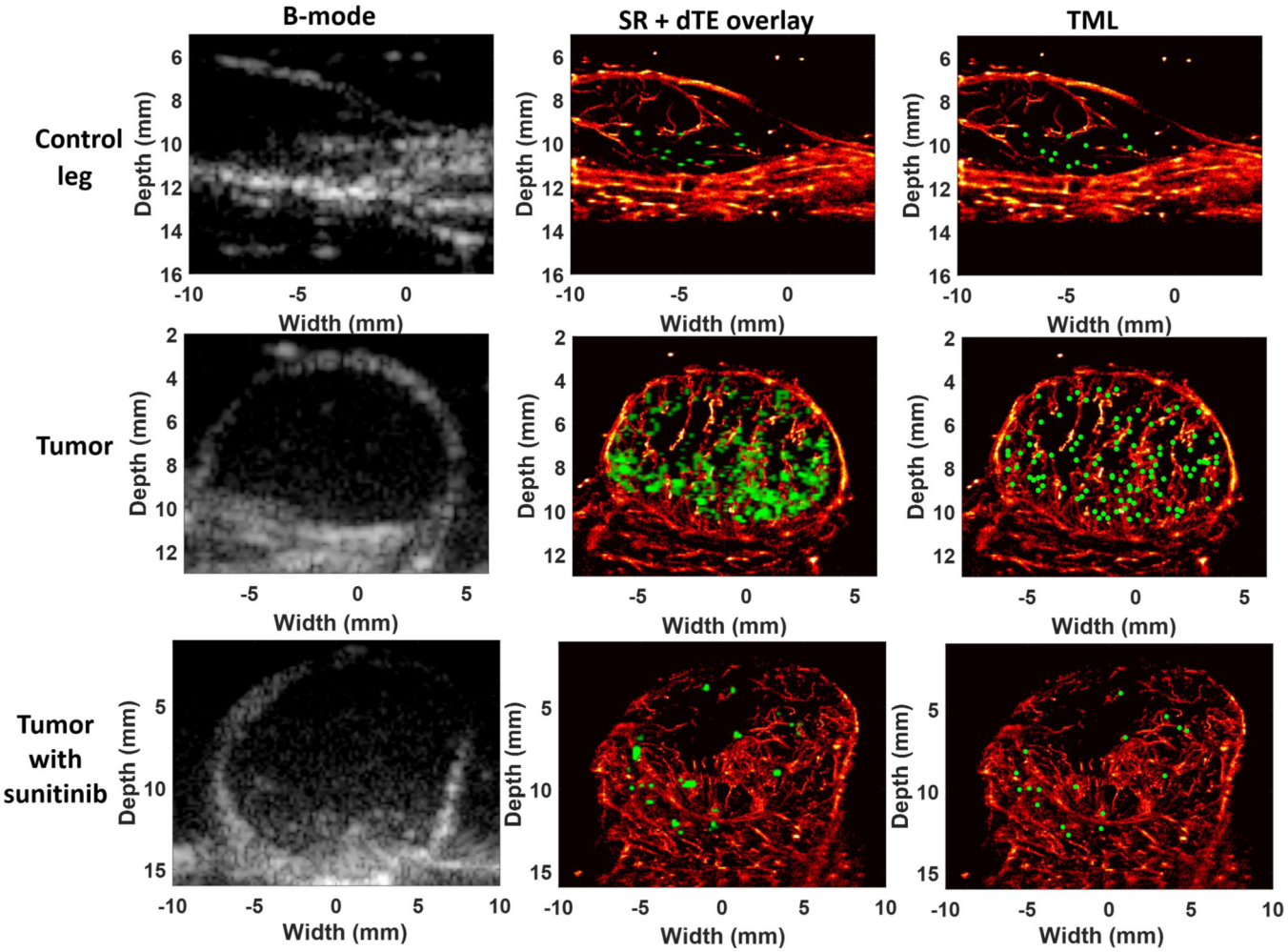

FIGURE 7.

Representative images of B-mode, SR + dTE overlay and TML for control leg, tumor and tumor with sunitinib, respectively. The dynamic range for B-mode images is 45 dB. The microvasculature is shown (in red) with co-localized adherent MBs signals (in green) by proposed method.

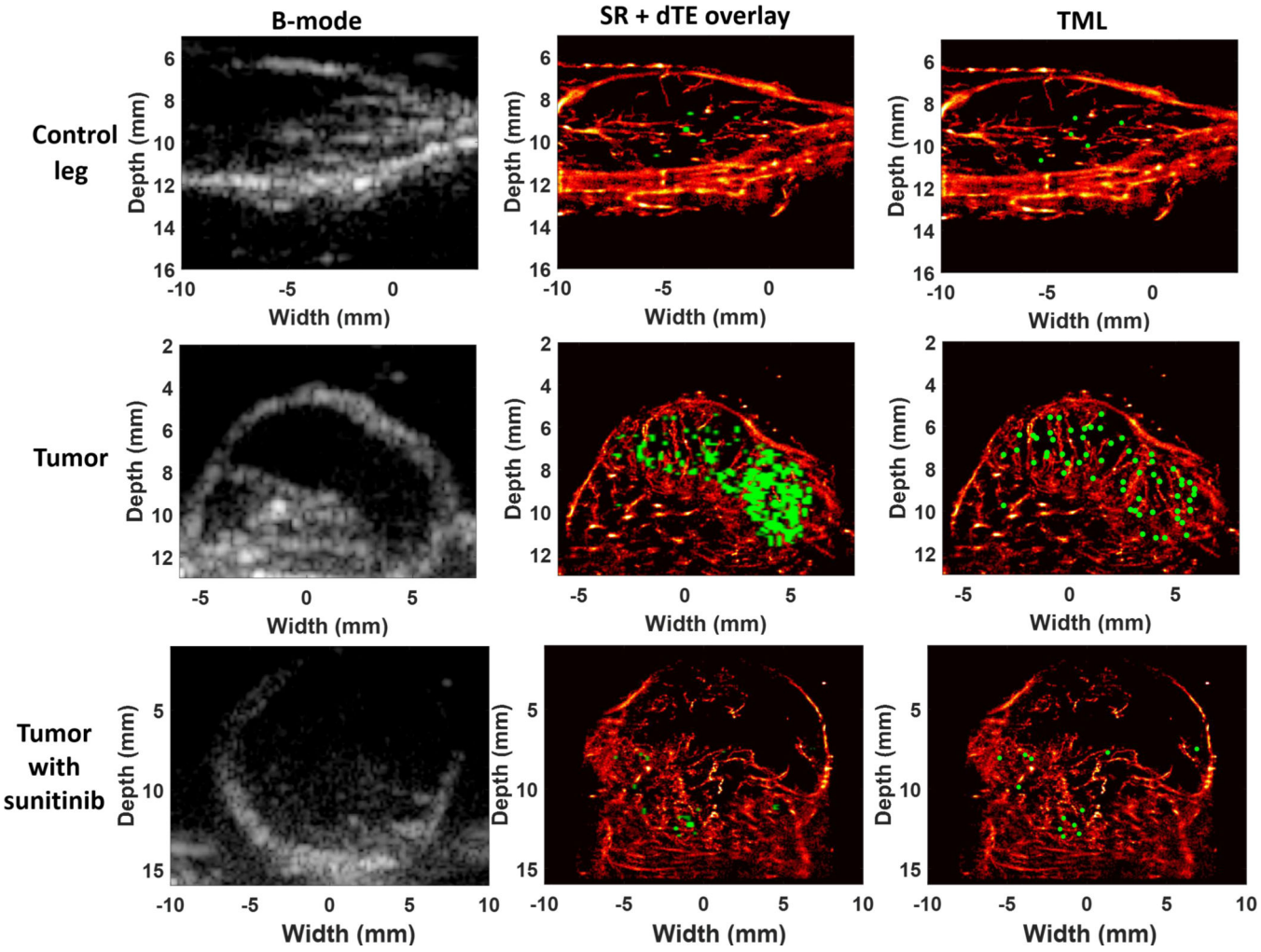

FIGURE 8.

Representative images of B-mode, SR + dTE overlay and TML for control leg, tumor and tumor with sunitinib, respectively, for another case. The dynamic range for B-mode images is 45 dB. The microvasculature is shown (in red) with co-localized adherent MBs signals (in green) using the proposed method.

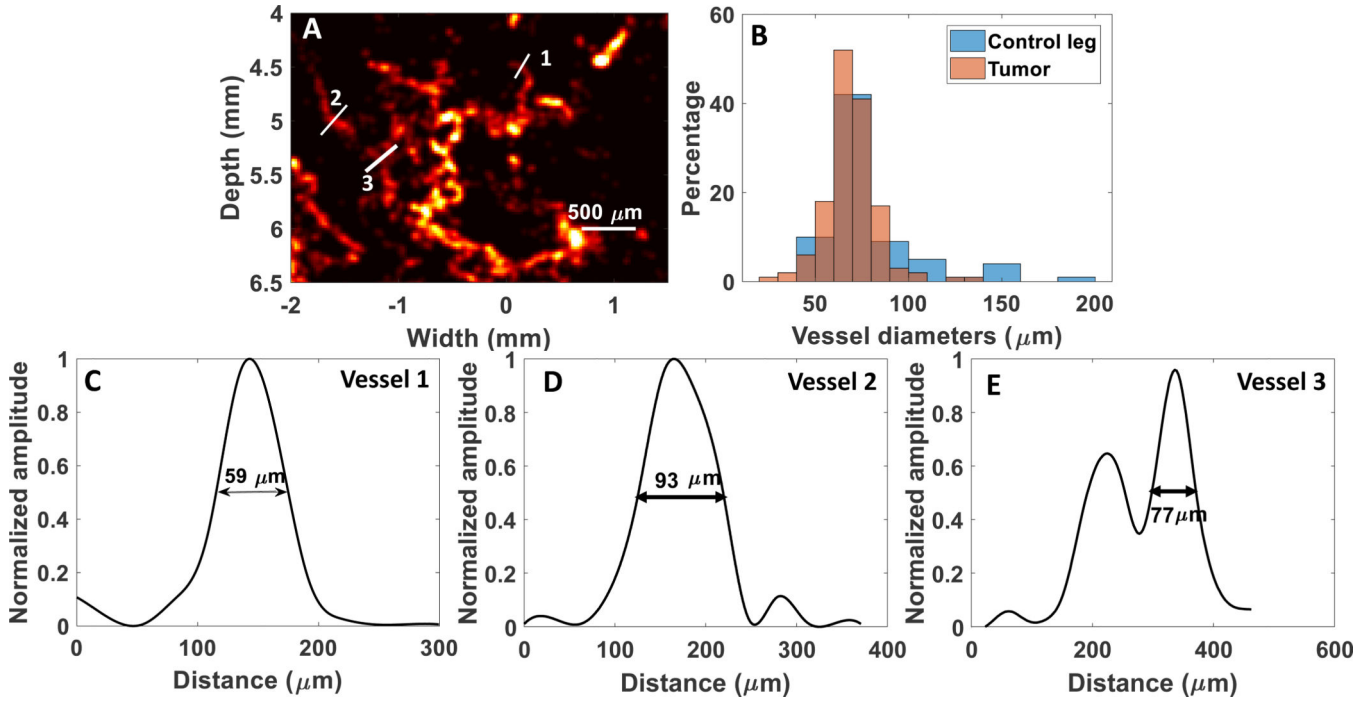

FIGURE 9.

(A) Microvessels of tumor resolved in super resolution, (C-E) the quantitative diameters of selected 3 vessels indicated by lines 1–3 in (A). (B) Histogram graph of vessel diameters corresponding to control leg and tumor respectively.

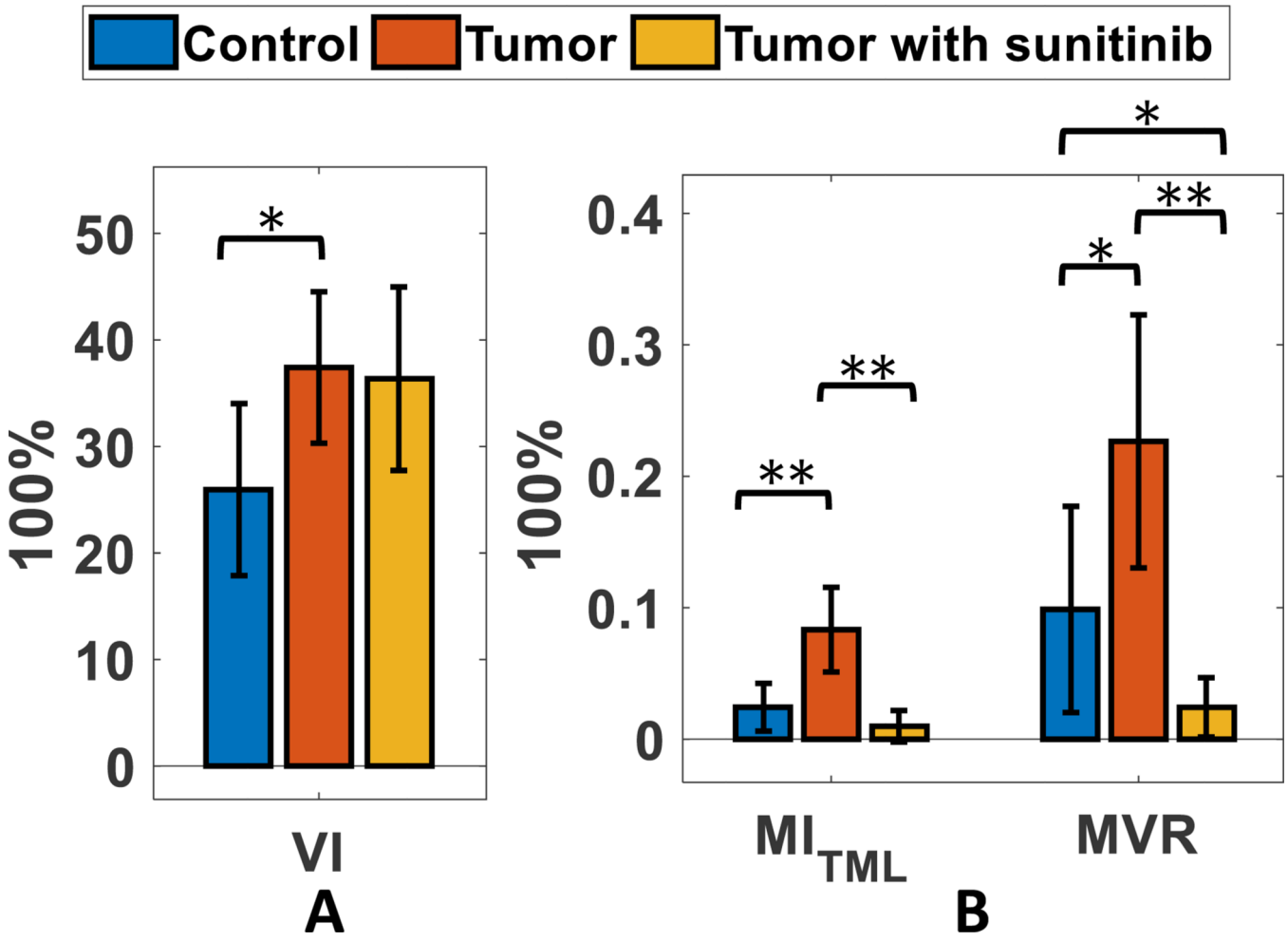

FIGURE 10.

Experiment quantification of (A) vascular index (VI), (B) molecular index (MI_{TML}) and molecular index to vessel surface ratio (MVR) from control leg, tumor, and tumor post-treatment groups averaged over six mice. * indicates $P < 0.05$, ** indicates $P < 0.01$. Error bars indicate standard deviation from the mean.

TABLE 1.

Summary of detected vessel diameters by TML approach

	Control leg	Tumor
Minimum	50.8 μm	28.8 μm
Maximum	196 μm	133.6 μm
Mean ± SD	80 ± 26 μm	69.4 ± 13 μm

SD, standard deviation.